Eur. Phys. J. E (2014) **37**: 60
DOI 10.1140/epje/i2014-14060-y

THE EUROPEAN PHYSICAL JOURNAL E

Regular Article

Rotational propulsion enabled by inertia

François Nadal[1,a], On Shun Pak[2], LaiLai Zhu[3,4], Luca Brandt[3], and Eric Lauga[5,b]

[1] Commissariat à l'Energie Atomique, 33114 Le Barp, France
[2] Department of Mechanical and Aerospace Engineering, Princeton University, Princeton, NJ, 08544-5263, USA
[3] Linné Flow Center, KTH Mechanics, S-100 44 Stockholm, Sweden
[4] Laboratory of Fluid Mechanics and Instabilities, EPFL, CH1015 Lausanne, Switzerland
[5] Department of Applied Mathematics and Theoretical Physics, University of Cambridge, Center for Mathematical Sciences, Wilberforce Road, Cambridge CB3 0WA, United Kingdom

Received 19 December 2013 and Received in final form 10 June 2014
Published online: 21 July 2014 –

Abstract. The fluid mechanics of small-scale locomotion has recently attracted considerable attention, due to its importance in cell motility and the design of artificial micro-swimmers for biomedical applications. Most studies on the topic consider the ideal limit of zero Reynolds number. In this paper, we investigate a simple propulsion mechanism —an up-down asymmetric dumbbell rotating about its axis of symmetry— unable to propel in the absence of inertia in a Newtonian fluid. Inertial forces lead to continuous propulsion for all finite values of the Reynolds number. We study computationally its propulsive characteristics as well as analytically in the small-Reynolds-number limit. We also derive the optimal dumbbell geometry. The direction of propulsion enabled by inertia is opposite to that induced by viscoelasticity.

1 Introduction

In the microscopic world, the physical forces we are used to experience on large scales come out in different proportions. In a fluid in particular, inertial forces tend to become smaller than viscous forces. This is why microfluidic devices, which enable fluid manipulations at length scales less than a millimeter, are dominated by the physics of viscous flows [1]. This affects, for example, the design of protocols for mixing liquids [2,3].

In the biological realm, the Reynolds numbers, Re, related to swimming microorganisms, such as bacteria and spermatozoa, lie in the range $\sim 10^{-2}$–10^{-5} [4, 5]. For these organisms, the absence of inertia leads to stringent constraints on the types of effective locomotion strategies, posing a fundamental challenge in the design of self-propelled micro- and nano-machines [5–8].

Most past studies in small-scale locomotion focused on the ideal limit of strictly zero Reynolds numbers, typically ignoring also the inertia of the swimmer. The governing equations in this limit are Stokes's equations, which are both linear and time-independent. These properties lead to so-called kinematic reversibility: an instantaneous reversing of the forcing does not modify the flow patterns, but only instantaneously reverses the direction of the flow [5]. A consequence of kinematic reversibility on locomotion in the Re $= 0$ limit is the so-called Purcell's scallop theorem [4], which rules out any reciprocal motion —deformations that are symmetrical under time reversal, such as simple flapping motions— for propulsion and fluid transport. Different strategies have since been proposed to escape from the constraints of the scallop theorem, including generating non-reciprocal deformation (such as the propagation of flagellar waves), exploiting non-Newtonian stresses, or inertial forces [9].

For any swimming cell or synthetic device, the Reynolds number is small but never strictly zero. It is therefore of fundamental physical interest to investigate the effects of small but finite inertia on small-scale locomotion. In particular, does inertia enhance or degrade propulsion of small objects, and can it be exploited? More fundamentally, how does the scallop theorem break down with inertia? The question was first posed by Childress and Dudley [10], who postulated that a finite amount of inertia was required to enable locomotion. Further investigations suggested that the breakdown of the scallop theorem with inertia depends on geometrical symmetries in the reciprocal actuation. Specifically, the breakdown is discontinuous for symmetric shapes [11–14], and continuous [15–17] for asymmetric shapes. In the context of cell motility, first inertial corrections to Taylor's swimming sheet model [18] were considered by Tuck [19] with an approach later simplified by Brennen [20]. Recently, two groups extended the classical squirmer model for ciliary propulsion for small values of Re [8,21].

[a] e-mail: francois.nadal33@gmail.com (corresponding author)
[b] e-mail: e.lauga@damtp.cam.ac.uk

In this paper, instead of quantifying the role of inertia on swimmers effective in the Stokes limit, we consider a simple steady mechanism unable to propel at Re = 0 in order to illustrate the first effect of inertia on propulsion. The system is an up-down asymmetric dumbbell, consisting of two spheres of different radii, made to rotate in a Newtonian fluid. Despite the geometrical asymmetry, such a dumbbell is unable to propel upon rotation about its axis of symmetry in a Newtonian fluid in the absence of inertia. This result can be shown by assuming without loss of generality that the dumbbell propels upward upon a clockwise rotation. By the kinematic reversibility of Stokes flows mentioned above, a counterclockwise rotation should then lead to a downward propulsion. However, the mirror image of the original configuration indicates that a dumbbell rotating in the counterclockwise direction should still propel upward. This contradiction leads to the conclusion that no propulsion is possible. The preceding argument requires the Reynolds number to be exactly zero, and here we show how inertia can enable propulsion at finite Reynolds number.

In classical work, Cox [22] showed that a rotating body lacking up-down symmetry, such as the asymmetric dumbbell considered in this paper, experiences a $O(\mathrm{Re})$ force along its symmetry axis. The asymmetric dumbbell geometry was recently proposed as a micro-propeller and microrheometer in viscoelastic fluids in the absence of inertia [23], and as will be discussed below, inertia and viscoelastic fluids lead to effects acting in opposite directions. Note that magnetically actuated asymmetric microdumbbells have been shown to propel in a purely Stokesian framework by Tierno *et al.* [24–26]. In this case, the propulsion, which is impossible to achieve in an isotropic medium, is enabled by the presence of a wall which breaks the symmetry of the nearby environment.

Our paper is organized as follows. Section 2 describes the geometric and kinematic setup of the problem. The results of numerical computations at moderate Reynolds numbers are presented in sect. 3. In sect. 4, we perform a linear perturbative analysis of the problem for small Reynolds number and obtain an integral expression for the propulsion speed. The propulsive characteristics of the rotating dumbbell are then investigated in sect. 5, where the optimal geometry is identified. The difference in nature between locomotion enabled by inertia and that caused by non-Newtonian effects is discussed in sect. 6. We conclude in sect. 7. Technical details about the different coordinate systems used to address the problem are given in appendices A and B.

2 Setup

The asymmetric dumbbell considered in this paper consists of two spheres of different sizes (radii R_1, R_2), whose centers lie on the z-axis at a distance H from each other ($H \geq R_1 + R_2$), as illustrated in fig. 1. In this work, we use capital letters for dimensional variables, and the corresponding dimensionless variables are denoted by small letters (this rule does not apply for constants). The two-sphere system is considered as a rigid body and both spheres rotate at the same steady angular velocity Ω about the z-axis. We thus suppose that a constant torque is applied to the body in order to ensure the constant rotation rate, but the net force on the body is assumed to be zero (force-free swimming). Except in sect. 7 where viscoelastic effects are also considered, the surrounding medium is a Newtonian fluid of density ρ_0 and dynamic viscosity μ. The kinematic viscosity is denoted as $\nu = \mu/\rho_0$. The surface of the sphere i ($i = 1, 2$) is referred to as $\mathcal{S}_i$ and $\mathcal{S} = \mathcal{S}_1 \cup \mathcal{S}_2$, with S_2 representing the large sphere. The entire volume of fluid is denoted by $\mathcal{V}$. By symmetry, the yet unknown translational propulsion velocity $\boldsymbol{V}$ induced by the rotation of the dumbbell can only be in the z-direction, $\boldsymbol{V} = V\,\boldsymbol{e}_z$. We aim at solving the problem in a particle-fixed frame of reference.

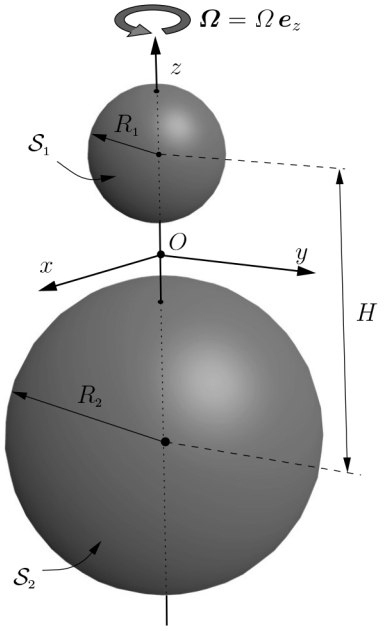

Fig. 1. Sketch of the geometry. The small sphere (radius R_1) is located on the positive z-axis and the large one (radius R_2) lies on the negative z-axis. The distance between the centers of the spheres is denoted H. The whole solid body (sphere 1 + sphere 2) rotates at the same angular velocity Ω, and H is kept constant. In the case of touching spheres we have $H = R_1 + R_2$.

The velocity and stress fields, $\{\boldsymbol{U}, \boldsymbol{\Sigma}\}$, satisfy the momentum and continuity equations

$$\boldsymbol{\nabla} \cdot \boldsymbol{\Sigma} = \rho_0 (\boldsymbol{U} \cdot \boldsymbol{\nabla})\, \boldsymbol{U}, \tag{1}$$

$$\boldsymbol{\nabla} \cdot \boldsymbol{U} = 0, \tag{2}$$

with the Newtonian constitutive equation

$$\boldsymbol{\Sigma} = -P\,\boldsymbol{\delta} + \mu[\boldsymbol{\nabla U} + \boldsymbol{\nabla U}^T], \tag{3}$$

where P is the pressure field and $\boldsymbol{\delta}$ is the unit tensor. In eq. (1), the time-dependent term has been omitted as we are interested in the steady limit only. Equations (1), (2) and (3) can be made dimensionless by using Ω^{-1}, R_2,

ΩR_2, and $\mu\Omega$ as typical time, length, velocity, and stress respectively, and one obtains

$$\boldsymbol{\nabla}\cdot\boldsymbol{\sigma} = \mathrm{Re}\,(\boldsymbol{u}\cdot\boldsymbol{\nabla})\boldsymbol{u}, \tag{4}$$

$$\boldsymbol{\nabla}\cdot\boldsymbol{u} = 0 \tag{5}$$

and

$$\boldsymbol{\sigma} = -p\,\boldsymbol{\delta} + [\boldsymbol{\nabla}\boldsymbol{u} + \boldsymbol{\nabla}\boldsymbol{u}^T]. \tag{6}$$

In eq. (4), the Reynolds number is given by

$$\mathrm{Re} = \Omega R_2^2/\nu. \tag{7}$$

Using the above non-dimensionalization, the dimensionless radius of the large sphere is unity and that of the small sphere is therefore given by the ratio $r = R_1/R_2$. The dimensionless distance between the centers of the spheres is denoted by $h = H/R_2$. The dimensionless translational propulsion velocity is denoted $\boldsymbol{v} = \boldsymbol{V}/\Omega R_2 = v\,\boldsymbol{e}_z$, with amplitude v.

Observing the motion in a reference frame moving with the dumbbell at $\boldsymbol{v} = v\,\boldsymbol{e}_z$ along the z-axis, the boundary conditions are given by

$$\begin{aligned} &\boldsymbol{u} = \rho\,\boldsymbol{e}_\phi \quad \text{on } \mathcal{S},\\ &\boldsymbol{u} \to -\boldsymbol{v} \quad \text{at infinity,} \end{aligned} \tag{8}$$

where $\boldsymbol{e}_\phi$ is the (cylindrical) azimuthal unit vector and $\rho = (x^2+y^2)^{1/2}$ is the distance to the z-axis.

In the following sections, we first consider numerical simulations at moderate Reynolds numbers (sect. 3), followed by a perturbative analysis in the small-Reynolds-number regime (sect. 4).

3 Inertial effects at moderate Reynolds numbers: Simulations

We first investigate the effect of inertia on the locomotion of the rotating dumbbell for a specific geometry. We consider two touching spheres (so $h = 1 + r$) of radii ratio $r = 0.5$. The numerical solution to eqs. (4) and (5) is implemented in COMSOL©, as it was in previous work studying locomotion and rheology at microscopic scales [23,27]. A two-dimensional rectangular domain with axisymmetric boundary conditions is considered. We have Dirichlet velocity boundary condition for the inlet, and pressure boundary condition for the outlet. The no-slip boundary condition is imposed on the rotating dumbbell. The bulk is discretized using triangle elements. Mesh resolution near the object is refined to properly capture the secondary flow, which is weaker than the main (rotational) flow by several orders. For validation, we computed the hydrodynamic force and torque exerted on a translating and rotating sphere respectively. In both cases, the agreement between numerical and analytical results was excellent. As the flows addressed here occur at small or moderate values of the Reynolds number, they are long-ranged and devoid of any boundary layers, and therefore numerical accuracy is more sensitive to the size of domain than to the mesh resolution. With careful tuning, a domain of size 1200×1200 (in units of the large sphere radius) is employed.

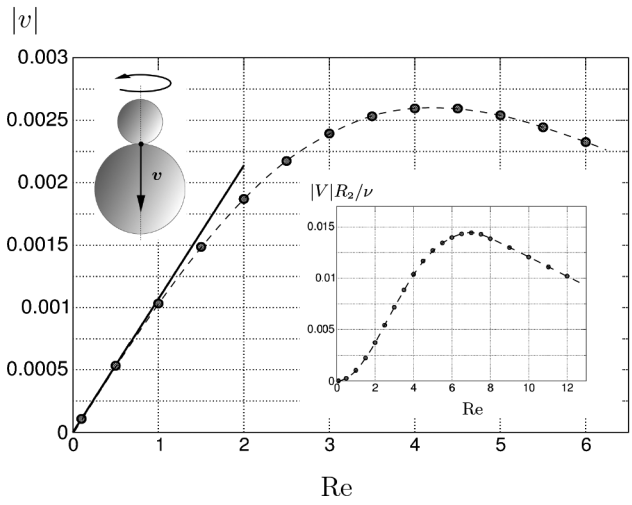

Fig. 2. Norm of the dimensionless propulsion speed, $|v|$, as a function of the Reynolds number, Re, for a dumbbell consisting of touching spheres with a radii ratio $r = 0.5$. Inset: $|V|R_2/\nu = |v|\,\mathrm{Re}$ is plotted as a function of the Reynolds number (alternative choice for the non-dimensionalization). The dashed line is a guide for the eye. The propulsion speed obtained analytically at small Reynolds number using a perturbative approach in sect. 4 is plotted as a solid line.

The simulations were performed in a reference frame translating with the dumbbell thus aims at determining the unknown inlet velocity, opposite to the propulsion velocity of the dumbbell in the laboratory frame. Numerically, we compute the force on the body as a function of the inlet velocity and then determine the inlet velocity satisfying the force-free condition via interpolation.

The computational results are displayed in figs. 2 and 3. We find that the propulsion velocity, $\boldsymbol{v}$, is always negative indicating that the dumbbell is moving with the large sphere ahead, independently of the rotational direction. The norm of the propulsion velocity, $|v|$, is plotted as a function of the Reynolds number in fig. 2. On the same figure, the solid line shows the results obtained with our perturbative analysis detailed in sect. 4. The agreement between the analysis and the computations is good for $\mathrm{Re} \lesssim 1$. Our computations show that the dimensionless propulsion speed displays a maximum around $\mathrm{Re} = 4.2$.

Since the value of the angular velocity, Ω, appears in both the Reynolds number and the non-dimensionalization for v, it is not obvious if the existence of this dimensionless maximum propulsion also leads to a dimensional maximum. Instead of ΩR_2 we non-dimensionalize v by ν/R_2, the magnitude of which is plotted in the inset of fig. 2. For a given geometry and fluid, we therefore see that a maximum still exists. The optimal Reynolds number with this new non-dimensionalization occurs around $\mathrm{Re} = 7$.

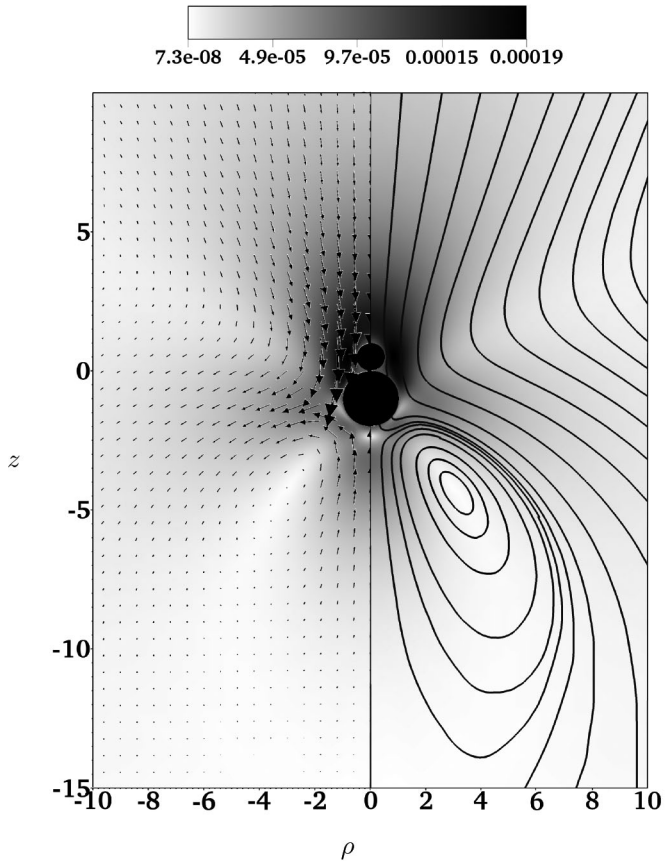

Fig. 3. Streamlines, velocity field, and magnitude in the laboratory frame of the dimensionless secondary flow (equal to the total flow minus the Stokes component), in the case of touching spheres, for $\mathrm{Re} = 0.1$ and a radii ratio $r = 0.5$.

In fig. 3 we plot the streamlines and velocity field in the laboratory frame of the inertial secondary flow, *i.e.* the difference between the total flow and the primary Stokes flow, for $\mathrm{Re} = 0.1$ and $r = 0.5$. The colormap quantifies the local fluid speed. In contrast to the secondary flow in the viscoelastic case [23], the fluid is drawn from infinity along the z-axis and then radially expelled around the dumbbell. A ring vortex is detected close to the large sphere, which breaks the top-down symmetry of the flow. At a Reynolds number of 0.1, the maximum speed of the secondary flow is around 0.02% of the typical speed ΩR_2.

4 Inertial effects at small Reynolds number

In this section, we derive an analytical expression for the propulsion speed, $\boldsymbol{v}$, valid in the limit of small Reynolds numbers. We consider the disturbance velocity field $\boldsymbol{u}' = \boldsymbol{u} - (-\boldsymbol{v})$ relative to the undisturbed uniform background flow $-\boldsymbol{v}$, due to the motion of the reference frame. The governing equations for the disturbance flow are

$$\boldsymbol{\nabla}\cdot\boldsymbol{\sigma}' = \mathrm{Re}\,\left[(\boldsymbol{u}'\cdot\boldsymbol{\nabla})\,\boldsymbol{u}' + (\boldsymbol{u}'\cdot\boldsymbol{\nabla})\,\boldsymbol{v} + (\boldsymbol{v}\cdot\boldsymbol{\nabla})\,\boldsymbol{u}'\right], \quad (9)$$

$$\boldsymbol{\nabla}\cdot\boldsymbol{u}' = 0, \quad (10)$$

where the disturbance stress field is equal to $\boldsymbol{\sigma}' = \boldsymbol{\sigma}$, since the undisturbed background flow contributes no additional stress. The boundary conditions for the disturbance flow are given by

$$\boldsymbol{u}' = \rho\,\boldsymbol{e}_\phi - (-\boldsymbol{v}) \quad \text{on } \mathcal{S},$$
$$\boldsymbol{u}' \to \boldsymbol{0} \quad \text{at infinity.} \quad (11)$$

In eq. (9), the term $(\boldsymbol{u}'\cdot\boldsymbol{\nabla})\boldsymbol{v}$ is identically zero since $\boldsymbol{v}$ is uniform. Hereafter, we drop the primes for notation convenience; all field variables below correspond to the disturbance flow unless otherwise stated.

We are interested in computing the first inertial effects in Reynolds number for a rotating dumbbell. In the case of uniform flow past a sphere, the inclusion of inertial effects leads to Whitehead's paradox [28], where the advective terms cannot be uniformly neglected and an Oseen analysis is necessary in the far field [29]. Whitehead's paradox does not however extend to a rotating sphere as the Stokes velocity field decays sufficiently fast [30], and a the flow can be addressed using regular perturbations [22,31,32]. We thus choose to expand the disturbance velocity and stress fields and the propulsion velocity of the rotating dumbbell as regular perturbation series in powers of the Reynolds number

$$\boldsymbol{u} = \boldsymbol{u}^{(0)} + \mathrm{Re}\,\boldsymbol{u}^{(1)} + O(\mathrm{Re}^2), \quad (12)$$

$$\boldsymbol{\sigma} = \boldsymbol{\sigma}^{(0)} + \mathrm{Re}\,\boldsymbol{\sigma}^{(1)} + O(\mathrm{Re}^2), \quad (13)$$

$$\boldsymbol{v} = \boldsymbol{v}^{(0)} + \mathrm{Re}\,\boldsymbol{v}^{(1)} + O(\mathrm{Re}^2). \quad (14)$$

Introducing the expansions (12) and (13) in the Navier Stokes equations leads to governing equations and boundary conditions at different orders. We analyze the problem order by order in the following sections.

4.1 Zeroth-order solution

The zeroth-order flow field satifies the Stokes equation

$$\boldsymbol{\nabla}\cdot\boldsymbol{\sigma}^{(0)} = 0, \quad (15)$$

$$\boldsymbol{\nabla}\cdot\boldsymbol{u}^{(0)} = 0, \quad (16)$$

with the following boundary conditions

$$\boldsymbol{u}^{(0)} = \rho\,\boldsymbol{e}_\phi + \boldsymbol{v}^{(0)} \quad \text{on } \mathcal{S}, \quad (17)$$

$$\boldsymbol{u}^{(0)} \to \boldsymbol{0} \quad \text{at infinity.} \quad (18)$$

The angular velocity of the dumbbell is of $O(1)$ and is entirely taken into account in the zeroth-order boundary conditions. It will thus not contribute to the boundary conditions at higher orders.

The Stokes flow problem posed by the equation at order zero was analyzed for separated [33] and touching [34] rotating spheres. No translational propulsion speed is obtained at the zeroth-order, $\boldsymbol{v}^{(0)} = \boldsymbol{0}$. This was to be expected by considering the time-reversal transformation and the mirror image of the original kinematics; they have identical kinematics but give opposite predictions on the direction of propulsion, hence no propulsion can occur.

4.2 First-order solution

The third nonlinear term on the right-hand side of eq. (9) has no contribution to the governing equation at $O(\mathrm{Re})$, since the propulsion velocity $\boldsymbol{v}$ is expected to be of $O(\mathrm{Re})$ at best. At first order, the governing equations become

$$\boldsymbol{\nabla}\cdot\boldsymbol{\sigma}^{(1)} = (\boldsymbol{u}^{(0)}\cdot\boldsymbol{\nabla})\,\boldsymbol{u}^{(0)}, \tag{19}$$

$$\boldsymbol{\nabla}\cdot\boldsymbol{u}^{(1)} = 0, \tag{20}$$

with boundary conditions

$$\boldsymbol{u}^{(1)} = \boldsymbol{v}^{(1)} \quad \text{on } \mathcal{S}, \tag{21}$$

$$\boldsymbol{u}^{(1)} \to \boldsymbol{0} \quad \text{at infinity.} \tag{22}$$

In theory, one could solve successively eqs. (15–16) and (19)–(20), integrate the stress at the surface of each sphere, and deduce the value of the propulsion velocity, $\boldsymbol{v}^{(1)}$, leading to zero net force. Alternatively, in order to bypass the detailed calculations, we use a modified version of Lorentz's reciprocal theorem in order to derive an expression for the propulsion velocity [35]. This approach was initially used by to compute the effect of inertia on the Stokes resistance of rigid particles [22,36], their migration in Poiseuille flows [37] and in arbitrary two-dimensional unidirectional flows [38] (Segré-Silbreberg effect).

4.3 Propulsion speed and external force

In order to apply the reciprocal theorem, we consider an auxiliary Newtonian Stokes problems with the same geometry but different boundary conditions satisfying the incompressible equations of mechanical equilibrium

$$\boldsymbol{\nabla}\cdot\hat{\boldsymbol{\sigma}} = \boldsymbol{0}, \tag{23}$$

$$\boldsymbol{\nabla}\cdot\hat{\boldsymbol{u}} = 0. \tag{24}$$

Subtracting the inner product of eq. (19) with $\hat{\boldsymbol{u}}$ and the inner product of eq. (23) with $\boldsymbol{u}^{(1)}$, and integrating over the volume of fluid $\mathcal{V}$ leads to the statement of equality of virtual powers

$$\int_{\mathcal{V}} \left[\hat{\boldsymbol{u}}\cdot(\boldsymbol{\nabla}\cdot\boldsymbol{\sigma}^{(1)}) - \boldsymbol{u}^{(1)}\cdot(\boldsymbol{\nabla}\cdot\hat{\boldsymbol{\sigma}})\right]\mathrm{d}\mathcal{V} = \int_{\mathcal{V}} \hat{\boldsymbol{u}}\cdot\left[(\boldsymbol{u}^{(0)}\cdot\boldsymbol{\nabla})\,\boldsymbol{u}^{(0)}\right]\mathrm{d}\mathcal{V}. \tag{25}$$

Then, using the general vector identity

$$\begin{aligned}\hat{\boldsymbol{u}}\cdot(\boldsymbol{\nabla}\cdot\boldsymbol{\sigma}^{(1)}) - \boldsymbol{u}^{(1)}\cdot(\boldsymbol{\nabla}\cdot\hat{\boldsymbol{\sigma}}) = {}& \boldsymbol{\nabla}\cdot(\hat{\boldsymbol{u}}\cdot\boldsymbol{\sigma}^{(1)} - \boldsymbol{u}^{(1)}\cdot\hat{\boldsymbol{\sigma}}) \\ & +(\boldsymbol{\nabla}\boldsymbol{u}^{(1)} : \hat{\boldsymbol{\sigma}} - \boldsymbol{\nabla}\hat{\boldsymbol{u}} : \boldsymbol{\sigma}^{(1)}),\end{aligned} \tag{26}$$

and realizing that the second term on the right-hand side of eq. (26) vanishes if the Newtonian flows are assumed to have the same viscosity, we can re-write eq. (25) in the form

$$\int_{\mathcal{V}} \boldsymbol{\nabla}\cdot(\hat{\boldsymbol{u}}\cdot\boldsymbol{\sigma}^{(1)} - \boldsymbol{u}^{(1)}\cdot\hat{\boldsymbol{\sigma}})\mathrm{d}\mathcal{V} = \int_{\mathcal{V}} \hat{\boldsymbol{u}}\cdot\left[(\boldsymbol{u}^{(0)}\cdot\boldsymbol{\nabla})\,\boldsymbol{u}^{(0)}\right]\mathrm{d}\mathcal{V}. \tag{27}$$

Use of the divergence theorem yields

$$\int_{\mathcal{S}} \boldsymbol{n}\cdot\left(\hat{\boldsymbol{u}}\cdot\boldsymbol{\sigma}^{(1)} - \boldsymbol{u}^{(1)}\cdot\hat{\boldsymbol{\sigma}}\right)\mathrm{d}\mathcal{S} = -\int_{\mathcal{V}} \hat{\boldsymbol{u}}\cdot\left[(\boldsymbol{u}^{(0)}\cdot\boldsymbol{\nabla})\,\boldsymbol{u}^{(0)}\right]\mathrm{d}\mathcal{V}. \tag{28}$$

In order to make further progress, we then assume that the auxiliary problem corresponds to a solid-body motion with translational velocity denoted $\hat{\boldsymbol{v}}$ and no rotation. Its boundary conditions on $\mathcal{S}$ are thus written

$$\hat{\boldsymbol{u}} = \hat{\boldsymbol{v}}, \tag{29}$$

where $\boldsymbol{r}$ is the position vector relative to the origin. Reminding that $\boldsymbol{v}^{(1)}$ is the first-order propulsion speed and introducing eqs. (21) and (29) in eq. (28), one gets

$$\hat{\boldsymbol{v}}\cdot\int_{\mathcal{S}} \boldsymbol{n}\cdot\boldsymbol{\sigma}^{(1)}\,\mathrm{d}\mathcal{S} - \boldsymbol{v}^{(1)}\cdot\int_{\mathcal{S}} \boldsymbol{n}\cdot\hat{\boldsymbol{\sigma}}\,\mathrm{d}\mathcal{S} = -\int_{\mathcal{V}} \hat{\boldsymbol{u}}\cdot\left[(\boldsymbol{u}^{(0)}\cdot\boldsymbol{\nabla})\,\boldsymbol{u}^{(0)}\right]\mathrm{d}\mathcal{V}. \tag{30}$$

In eq. (30), the first term of the left-hand side is the inner product of the auxiliary translational velocity of the solid body, with the force $\boldsymbol{f}^{(1)} = \int_{\mathcal{S}} \boldsymbol{n}\cdot\boldsymbol{\sigma}^{(1)}\,\mathrm{d}\mathcal{S}$ applied by the first-order flow in the main problem while the second term is similar with the role of the flows reversed. Denoting by $\hat{\boldsymbol{f}}$ the force applied by the auxiliary flow on the solid body, we obtain a convenient form of eq. (30) as

$$\hat{\boldsymbol{v}}\cdot\boldsymbol{f}^{(1)} - \boldsymbol{v}^{(1)}\cdot\hat{\boldsymbol{f}} = -\int_{\mathcal{V}} \hat{\boldsymbol{u}}\cdot\left[(\boldsymbol{u}^{(0)}\cdot\boldsymbol{\nabla})\,\boldsymbol{u}^{(0)}\right]\mathrm{d}\mathcal{V}. \tag{31}$$

Equation (31) can be used to compute two different quantities of interest. For a force-free dumbbell, we can use it to compute the propulsion speed, $\boldsymbol{v}^{(1)}$. Alternatively it can be exploited to compute the force applied by the fluid $\boldsymbol{f}^{(1)}$ on a non-translating dumbbell (which is equal to minus the external force required to prevent the dumbbell from moving). In both cases, the most appropriate candidate for the auxiliary problem is the flow induced by a translation along the dumbbell axis. In the free-swimming case we have $\boldsymbol{f}^{(1)} = \boldsymbol{0}$, and eq. (31) becomes

$$\boldsymbol{v}^{(1)}\cdot\hat{\boldsymbol{f}} = \int_{\mathcal{V}} \hat{\boldsymbol{u}}\cdot[(\boldsymbol{u}^{(0)}\cdot\boldsymbol{\nabla})\,\boldsymbol{u}^{(0)}]\mathrm{d}\mathcal{V}. \tag{32}$$

For a non-translating dumbbell we have $\boldsymbol{v}^{(1)} = \boldsymbol{0}$, and therefore the fluid force can be computed using

$$\hat{\boldsymbol{v}}\cdot\boldsymbol{f}^{(1)} = -\int_{\mathcal{V}} \hat{\boldsymbol{u}}\cdot[(\boldsymbol{u}^{(0)}\cdot\boldsymbol{\nabla})\,\boldsymbol{u}^{(0)}]\mathrm{d}\mathcal{V}. \tag{33}$$

In the following, we focus on the case of force-free propulsion. Both vectors $\boldsymbol{v}^{(1)}$ and $\hat{\boldsymbol{f}}$ are aligned with the z-direction. If we assume, without loss of generality, that $\hat{\boldsymbol{v}}$ is positively oriented on the z-axis, then

$$\hat{\boldsymbol{f}} = -|\hat{\boldsymbol{f}}|\,\boldsymbol{e}_z, \tag{34}$$

and from eq. (32) we obtain explicitly the first-order propulsion speed as

$$\boldsymbol{v}^{(1)} = -|\hat{\boldsymbol{f}}|^{-1}\left[\int_{\mathcal{V}} \hat{\boldsymbol{u}}\cdot[(\boldsymbol{u}^{(0)}\cdot\boldsymbol{\nabla})\,\boldsymbol{u}^{(0)}]\mathrm{d}\mathcal{V}\right]\boldsymbol{e}_z. \tag{35}$$

In this final equation, it should be noted that the propulsion velocity of the dumbbell, $\boldsymbol{v}^{(1)}$, does not depend on the magnitude of the translational velocity in the auxiliary problem, $\hat{\boldsymbol{v}}$, since both the auxiliary force, $\hat{\boldsymbol{f}}$, and the velocity field, $\hat{\boldsymbol{u}}$, scale linearly with $\hat{\boldsymbol{v}}$. Similarly, the force experienced by the solid body from the fluid, in eq. (33), does not depend on the magnitude of the auxiliary translational velocity. In fig. 2, the results given by this perturbative analysis are shown in solid line and compared to the computational results (symbols) for a dumbbell consisting of a touching sphere with a radii ratio $r = 0.5$. We observe good agreement in the small-Reynolds-number regime ($\mathrm{Re} \lesssim 1$).

5 Geometric optimization

We now turn to the calculation of the optimal geometry for a dumbbell. Specifically, we use our analytical calculation and eq. (35) to determine the radii ratio and the distance between the centers for which the propulsion speed is the highest. The problems of a dumbbell consisting of touching spheres (sect. 5.1) and separated spheres (sect. 5.2) are considered separately. For separated spheres, the solution to the auxiliary problem was given by Stimson and Jeffrey [39] in form of a series, which converges slowly as the spheres get closer to each other. For touching spheres, we adopt the solution given by Takagi [34] for the auxiliary problem.

5.1 Touching spheres

To address the problem of the touching-sphere configuration, it is convenient to use tangent-sphere coordinates system (see appendix A.1). Considering the expression of the integrand involved in the right-hand side of eq. (35), we have to derive the expression of the auxiliary Stokes flow $\hat{\boldsymbol{u}}$ induced by a simple translation along the center line of the spheres and the convective term $(\boldsymbol{u}^{(0)}\cdot\boldsymbol{\nabla})\,\boldsymbol{u}^{(0)}$, where $\boldsymbol{u}^{(0)}$ is the Stokes flow induced by a simple rotation of the dumbbell about the center line of spheres. The expression of the auxiliary stream function for translational touching spheres has been given by Cooley and O'Neil [33]. The expression of the velocity field $\hat{\boldsymbol{u}}$ in terms of tangent-sphere coordinates is derived in appendix A.2, where the drag in the auxiliary problem $\hat{\boldsymbol{f}}$ is also included.

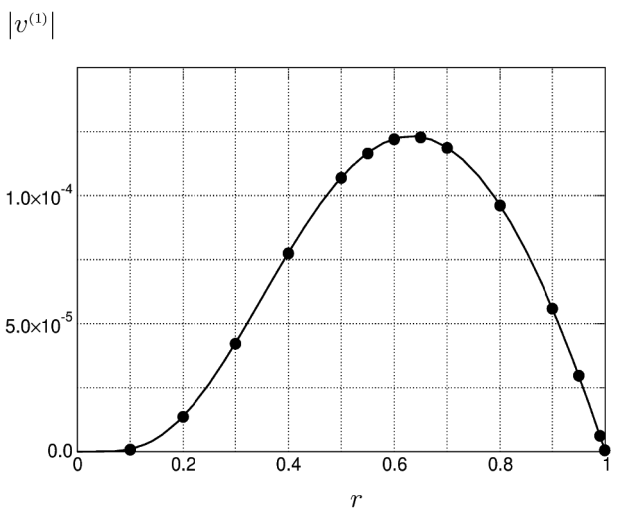

Fig. 4. Norm of the first-order propulsion speed, $|v^{(1)}|$, as a function of the ratio of radii, r, for two rotating touching spheres. Numerical results computed for $\mathrm{Re} = 0.1$ and analytical results are plotted with circles and a solid line, respectively.

The Stokes flow induced by two rotating touching spheres was found by Takagi [34]. The expression of the convective term as a function of tangent-sphere coordinates is then given in appendix A.3.

With eqs. (A.4), and (A.20)–(A.23), we perform the numerical integration in eq. (35) and obtain the amplitude of the first-order propulsion speed $v^{(1)}$ (see details in appendix A.4). For all geometries considered, we find that $v^{(1)} < 0$, and locomotion occurs with the larger sphere ahead. The optimization of the touching-spheres geometry is presented in fig. 4. In the latter is plotted the norm of the first-order propulsion speed, $|v^{(1)}|$, as a function of the radii ratio. The results given by linear perturbative analysis are in good agreement with the numerical simulations computed for $\mathrm{Re} = 0.1$. The presence of an optimum (around $r = 0.63$) can be understood since the propulsion speed vanishes for a symmetric dumbbell ($r \to 1$) and for a single sphere ($r \to 0$) by symmetry.

5.2 Separated spheres

We now let the spheres separate from each other at a distance $h > 1 + r$, while still assuming they both rotate with the same angular velocity. The approach is similar to the case of touching spheres. We need two Stokes flows. For the zeroth-order problem we need the solution for two separated spheres rotating at the same angular velocity about their centerline given by Jeffery [40]. For the auxiliary problem we need the solution for two separated spheres translating at the same velocity along their centerline, whose solution is given by Stimson and Jeffery [39]. Using eqs. (B.6), (B.15)–(B.16), and (B.21)–(B.22), we evaluate the integral in eq. (35) numerically and obtain the first-order propulsion speed, $v^{(1)}$, for the

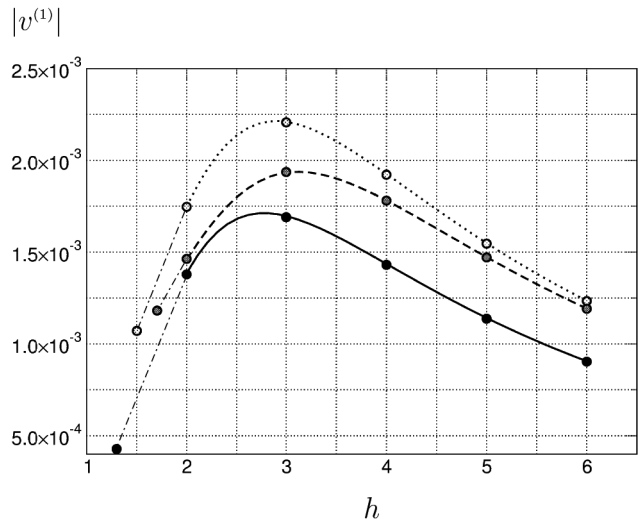

Fig. 5. Norm of first-order propulsion speed, $|v^{(1)}|$, as a function of the separation distance, h, for three different ratios of radii. Analytical results are plotted with lines and numerical results with Re = 0.1 in circles. Results are for $r = 0.3$ (solid line and black solid circles), $r = 0.5$ (dotted line and grey solid circles), and $r = 0.7$ (dashed line and open circles).

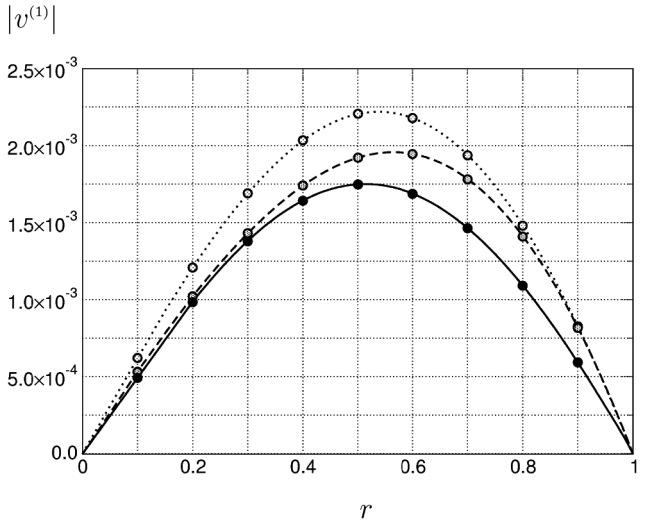

Fig. 6. Norm of the first-order propulsion speed, $|v^{(1)}|$, as a function of the radii ratio, r, for three different separation distances. Analytical results are plotted with lines and numerical results for Re = 0.1 using circles. Results are for $h = 2$ (solid line and black solid circles), $h = 3$ (dotted line and grey solid circles), and $h = 4$ (dashed line and open circles).

case of separated spheres (see appendix B.4 for details of the numerical integration).

In fig. 5, the dimensionless velocity is plotted as a function of the separation distance, h, for three ratios $r = 0.3$, 0.5 and 0.7. As expected, the propulsion speed decays at large separation distances $h \gg 1$, since each sphere is then isolated and does not experience the flow induced by the rotation of the other. We observe, surprisingly, a non-monotonic variation of the propulsion velocity with the separation distance. This dependence may be rationalized by considering the secondary inertial flow generated by a single rotating sphere in the absence of the other sphere. Such an inertial secondary flow expels fluid along the direction of the equator and by continuity draws in fluids along the vertical direction (z-axis). When two rotating spheres are aligned vertically, the secondary flows due to their rotation act to attract the two spheres. The direction of propulsion is a result of the competition between the attractive force on each sphere. The secondary flow of a single rotating sphere has to vanish at infinity as well as on the surface of the sphere. An extremum in the flow velocity along the z-axis is therefore expected. As a consequence, the propulsion velocity could be optimal when the second sphere stands around the extremum, experiencing a strong attractive force. Note that the precise optimal separation distance also depends on the sizes of the two spheres, and two equal spheres lead to no propulsion.

The dimensionless propulsion velocity is shown in fig. 6 as a function of the radii ratio, r, for three different separation distances, $h = 2$, 3 and 4. We observe qualitatively the same behavior as in the case of touching spheres. As expected, the propulsion speed vanishes for a single sphere ($r = 0$) and a symmetric dumbbell ($r = 1$) by symmetry. However, it can be noticed that the propulsion velocity goes linearly to zero as r decreases to zero, whereas the decay is faster for touching spheres.

Since non-monotonic variations of the propulsion velocity are observed in both the radii ratio, r, and separation distance, h, we can expect the existence of a global optimal geometry $(r^\star, h^\star)$ for the maximal propulsion speed. Iso-contours of the norm of the first-order propulsion speed are plotted in the (r, h) plane in fig. 7 for Re = 0.1. The extremum located at $(r^\star, h^\star) = (0.53, 2.94)$ corresponds to the geometry with maximum propulsion speed per unit angular velocity. Note that in the linear regime, the value of each contour scales linearly with Re. The geometry of the contours, including the extremum, is therefore independent of the Reynolds number in the $\mathrm{Re} \ll 1$ regime.

6 Propulsion in a viscoelastic fluid with inertia

As shown by Pak *et al.* [23], the rotating dumbbell geometry is also able to swim in a viscoelastic fluid in the absence of inertia. Interestingly, the direction of propulsion in that case is opposite to the case of inertial propulsion in a Newtonian fluid, and swimming occurs there with the small sphere ahead. In an actual viscoelastic fluid, both effects are present, potentially counteracting each other. We analyze the combined effects of inertia and viscoelasticity in this section.

The retarded-motion expansion for non-Newtonian flows is an expansion about the Newtonian behavior, where successive terms in the expansion systematically account for the departures from Newtonian behavior due to elastic effects [41]. The second-order relationship between

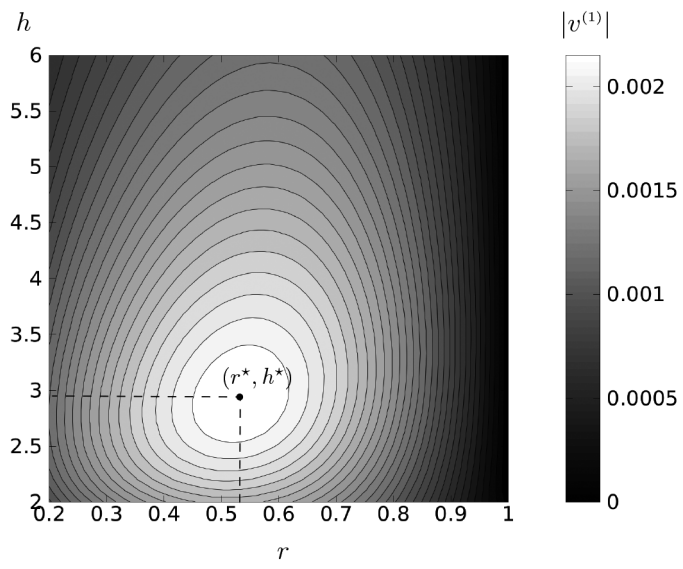

Fig. 7. Isovalues of the norm of the first-order propulsion speed, $|v^{(1)}|$, in the (r, h) plane. The optimal geometry is obtained for $(r^\star, h^\star) = (0.53, 2.94)$.

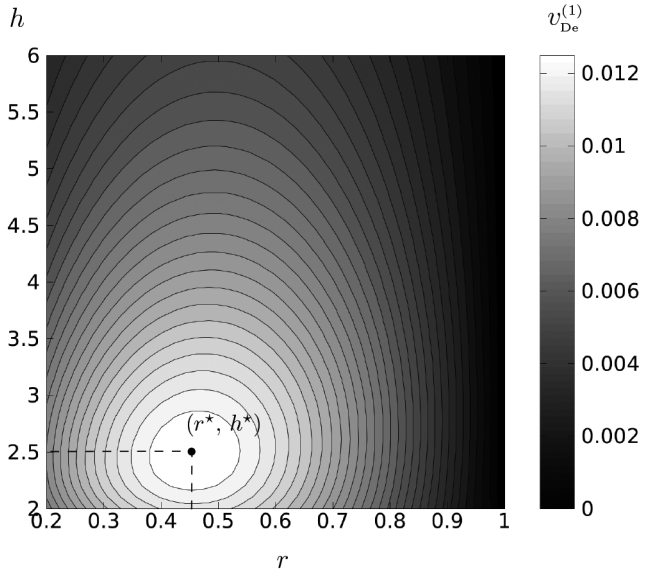

Fig. 8. Isovalues of the first-order propulsion speed amplitude, $v_{\mathrm{De}}^{(1)}$, in the case of a second-order viscoelastic fluid without inertia ($B = 0$). The optimal geometry is located at $(r^\star, h^\star) = (0.46, 2.5)$, and leads to swimming along the positive z direction.

stresses and rate-of-strain is the result of truncating the expansion after the second-order terms, and is valid when the velocity gradients are small. Since that expansion rigorously quantifies the first deviation from Newtonian fluid behavior, it has been extensively employed to solve a variety of flow problems [41].

The relationship between the total deviatoric stress, $\boldsymbol{T}$, and the the rate of strain, $\dot{\boldsymbol{\Gamma}}$, is given for a so-called second-order fluid by

$$\boldsymbol{T} = \eta\dot{\boldsymbol{\Gamma}} - \frac{1}{2}\Psi_1 \overset{\triangledown}{\dot{\boldsymbol{\Gamma}}} + \Psi_2\, \dot{\boldsymbol{\Gamma}} \cdot \dot{\boldsymbol{\Gamma}}, \tag{36}$$

where Ψ_1 and Ψ_2 are the first and second normal-stress coefficients respectively, and the upper-convected derivative of a tensor $\boldsymbol{A}$ is defined as

$$\overset{\triangledown}{\boldsymbol{A}} = \frac{\partial \boldsymbol{A}}{\partial t} + \boldsymbol{U} \cdot \boldsymbol{\nabla}\boldsymbol{A} - \left[\boldsymbol{\nabla}\boldsymbol{U}^T \cdot \boldsymbol{A} + \boldsymbol{A} \cdot \boldsymbol{\nabla}\boldsymbol{U}\right]. \tag{37}$$

The normal-stress coefficients, Ψ_1 and Ψ_2, quantify the extra normal stress generically arising in polymeric flows and responsible for many well-known phenomena such as rob-climbing and die-swelling of polymer melts [41,42]. In a Newtonian flow, there are no normal-stress differences ($\Psi_1 = \Psi_2 = 0$), whereas for polymeric fluids typically we have $\Psi_1 > 0$ and $\Psi_2 < 0$. The second normal-stress coefficient is usually much smaller in magnitude than that of the first normal-stress coefficient, *i.e.* $|\Psi_2| \ll \Psi_1$ [41].

Equation (36) can be made dimensionless by choosing the same typical quantities as in the Newtonian case (*i.e.* R_2, Ω^{-1}, $R_2\Omega$, Ω and $\eta\Omega$ for typical length, time, velocity, shear and stress respectively), and one gets

$$\boldsymbol{\tau} = \dot{\boldsymbol{\gamma}} - \mathrm{De}\left(\overset{\triangledown}{\dot{\boldsymbol{\gamma}}} + B\,\dot{\boldsymbol{\gamma}} \cdot \dot{\boldsymbol{\gamma}}\right), \tag{38}$$

where $\mathrm{De} = \Psi_1\Omega/2\eta$ is the Deborah number and $B = -2\Psi_2/\Psi_1$ is the normal-stress coefficient ratio. Since the second normal-stress coefficient is typically much smaller than the first normal-stress coefficient, $B \ll 1$ [41], we consider here the case $B = 0$ for simplicity.

After expanding the total stress, velocity and shear fields, and the propulsion velocity in powers of the Deborah number, and using again the reciprocal Lorentz theorem [23], one obtains the expression of the first-order viscoelastic propulsion speed in the absence of inertia, which is the viscoelastic equivalent of eq. (35) as

$$\boldsymbol{v}_{\mathrm{De}}^{(1)} = -|\hat{\boldsymbol{f}}|^{-1}\left[\int_{\mathcal{V}} \overset{\triangledown}{\dot{\boldsymbol{\gamma}}}^{(0)} : \boldsymbol{\nabla}\hat{\boldsymbol{u}}\,\mathrm{d}\mathcal{V}\right]\boldsymbol{e}_z. \tag{39}$$

The zeroth-order and auxiliary solutions in eq. (39) are the same as in the Newtonian cases. A map of isovalues of $v_{\mathrm{De}}^{(1)}$, magnitude of $\boldsymbol{v}_{\mathrm{De}}^{(1)}$, is reproduced in fig. 8.

Due to the linear nature of the perturbation analysis performed in both the viscoelastic and inertial cases, the dimensionless propulsion speed taking into account both effects can be obtained by summing up eq. (35) and eq. (39), leading to

$$\boldsymbol{v} = \mathrm{De}\,\boldsymbol{v}_{\mathrm{De}}^{(1)} + \mathrm{Re}\,\boldsymbol{v}_{\mathrm{Re}}^{(1)}. \tag{40}$$

A subscript Re has been added to the inertial first-order speed previously referred to as $\boldsymbol{v}^{(1)}$ to avoid any confusion between the inertial and viscoelastic speeds.

For a given fluid with fixed density, viscosity, normal-stress coefficient, and a typical size R_2, what is then the most efficient overall geometry? In other words, for which values of (r, h) does the dimensionless speed v, which includes both physical effects, have the largest amplitude?

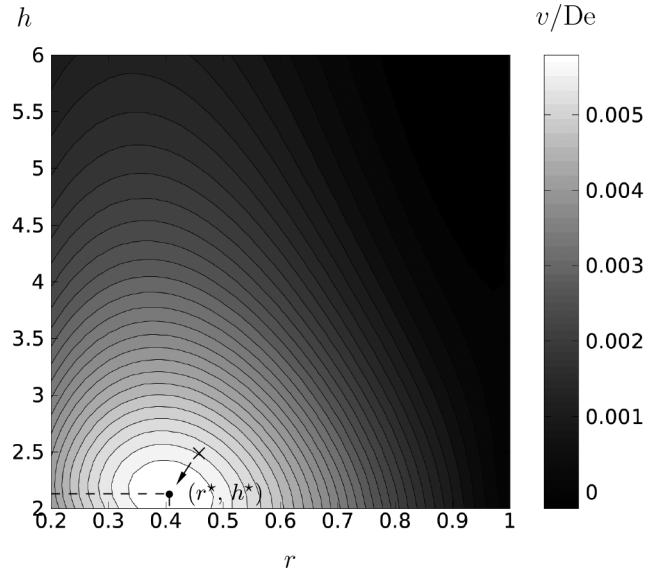

Fig. 9. Isovalues of the signed propulsion speed amplitude divided by the Deborah number, v/De, for a ratio $\chi = 3.5$. Viscoelasticity dominates and the optimal geometry is now located at $(r^\star, h^\star) = (0.41, 2.2)$, with swimming along the $+z$ direction. The optimal geometry in the absence of inertia from fig. 8 is shown using the symbol $\times$.

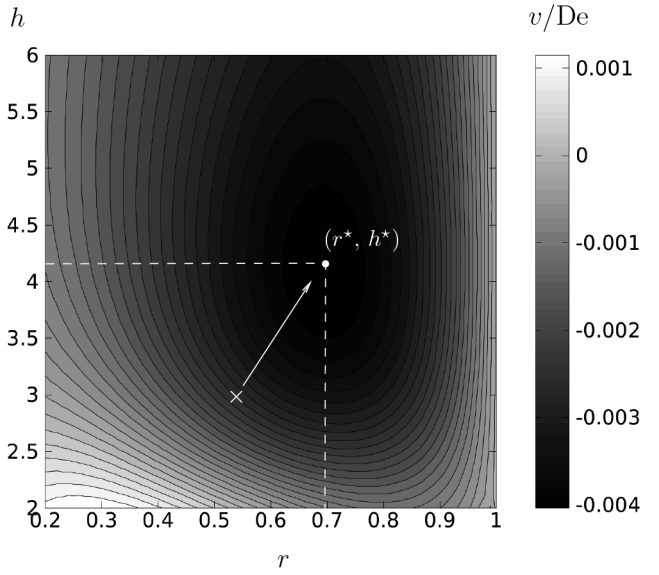

Fig. 10. Isovalues of the propulsion speed amplitude divided by the Deborah number, v/De, for a ratio $\chi = 6.5$. Inertial effects now dominate and optimal geometry is now located at $(r^\star, h^\star) = (0.69, 4.1)$, with swimming along the $-z$ direction. The optimal geometry in the absence of viscoelasticity from fig. 7 is shown by the symbol $\times$.

Denoting the fluid density ρ_0, the viscosity η, and normal-stress coefficient Ψ_1, and a dumbbell of given typical size R_2, then the ratio $\chi = \mathrm{Re}/\mathrm{De} = 2\rho_0 R_2^2/\Psi_1$ has a fixed value. Rewriting eq. (40) in the form

$$\frac{\boldsymbol{v}}{\mathrm{De}} = \boldsymbol{v}_{\mathrm{De}}^{(1)} + \chi \boldsymbol{v}_{\mathrm{Re}}^{(1)}, \tag{41}$$

we see that the optimal geometry depends on χ, as $\boldsymbol{v}_{\mathrm{De}}^{(1)}$ and $\boldsymbol{v}_{\mathrm{Re}}^{(1)}$ are not proportional to each other. This dependence is illustrated in figs. 9 and 10, which result from a linear combination of figs. 7 and 8. In fig. 9, isovalues of the amplitude of $\boldsymbol{v}$ on the z-axis are plotted in the (r, h) plane for $\chi = 3.5$. In this limit the viscoelastic effects are dominant as $v > 0$ but the optimal geometry is shifted relative to its position of $(0.46, 2.5)$ in the pure viscoelastic case. Conversely, for the value $\chi = 6.5$ shown in fig. 10, the inertial effects are dominant and $v < 0$, but the optimal geometry is also shifted relative to its position of $(0.53, 2.94)$ for the pure inertial Newtonian case.

Note that the optimization above ensues from our linear perturbation analysis in Reynolds and Deborah numbers, and therefore the results presented in figs. 9 and 10 are only valid in this asymptotic limit. In other words, we have only optimized the initial slope in fig. 2 and its viscoelastic equivalent. In order to derive the global optima, full numerical simulations should be employed.

7 Discussion and conclusion

For reciprocal motion at Reynolds number exactly equal to zero, Purcell's scallop theorem dictates that propulsion is impossible. With the inclusion of inertia, the transition from a non-swimmer to swimmer can occur either continuously or discontinuously with Reynolds number, depending on geometrical symmetries (see Introduction). In this paper we provide an example where the non-reciprocal motion (rotating dumbbell) is unable to produce propulsion in the absence of inertia due to mirror reflection symmetry. The geometry considered here is asymmetric (unequal spheres), and inertia in this case enables the locomotion continuously with the Reynolds number, consistently with past work. Interestingly, inertial forces enable locomotion for a non-chiral shape, whereas Stokesian locomotion of rigid bodies is typically associated with rigid, helical shapes.

A second result of interest is the contrast between inertial and viscoelastic effects. As a rule of thumb [41], the two effects seem to systematically give secondary flows of opposite directions, at least in the case of steady motion. Our results are consistent with this observation and a rotating dumbbell propels with the large (respectively, small) sphere ahead in a pure inertial (respectively, viscoelastic) fluid. In an experimental, both the inertial and viscoelastic effects are expected to be present. We performed a linear perturbative analysis for small Reynolds and Deborah numbers, and we showed how the optimal geometry of the dumbbell depends on the ratio of the Reynolds to the Deborah numbers (χ).

One question posed by the study is that of performance. How effective is inertia at propelling asymmetric objects? For the sake of comparison, let us contrast it here with a known propulsion mechanism in the absence of inertia, namely the rotation of helical flagella.

A swimming bacterium such as *E. coli*, which is near optimal in its geometrical design [43], swims at a speed of about $U \sim 30\,\mu\mathrm{m\,s}^{-1}$. With a total cell length $L \approx 10\,\mu\mathrm{m}$ and a flagellar rotational frequency of about $\Omega = 2\pi f$, with $f \approx 100\,\mathrm{Hz}$, this leads to the dimensionless speed per unit length $U/L\Omega \approx 1/200$. In the current paper, considering the optimal geometry obtained in fig. 7 ($r \approx 0.5$, $h \approx 2.9$) and assuming that the linear scaling seen in fig. 2 remains valid up to $\mathrm{Re} = 1$, we get $v^{(1)} \approx 2 \times 10^{-3}$, which, at $\mathrm{Re} = 1$, leads to a dimensionless velocity $v \approx 1/500$. Inertial propulsion leads therefore to performance of the same order as that seen in the biological realm.

The results presented here may be useful for the design of small-scale inertial propellers and pumps in Newtonian and complex fluids. The first correction of the propulsion speed due to inertia in a viscoelastic effect may also improve the accuracy of the measurement of the normal-stress coefficients of a complex fluid when the rotating dumbbell is used as a micro-rheometer [23].

The authors thank the Department of Mechanical and Aerospace Engineering at the University of California San Diego where this research was initiated. This work was funded in part by the Croucher Foundation through a Croucher Fellowship to OSP, the Seventh Framework Programme of the European Union through a Marie Curie grant to EL (Grant PCIG13-GA-2013-618323) and the Direction Générale de l'Armement (Grant 2012600091-Project ERE 12C0020).

Appendix A. Mathematics of touching spheres

In this section we present the technical details of the touching-spheres computations. We first recall the main characteristics of this particular coordinate system (expressions of the basis vectors etc.). We then give the expression of the auxiliary flow and drag in terms of tangent-sphere coordinates, followed by the derivation of the expression of the nonlinear advective term $(\boldsymbol{u}^{(0)} \cdot \boldsymbol{\nabla})\,\boldsymbol{u}^{(0)}$ involved in eq. (35).

Appendix A.1. Tangent-sphere coordinates

The tangent-sphere coordinate system is defined by the transformation

$$x = \frac{2\eta\cos\phi}{\xi^2+\eta^2}\,, \qquad y = \frac{2\eta\sin\phi}{\xi^2+\eta^2}\,, \qquad z = \frac{2\xi}{\xi^2+\eta^2}\,, \tag{A.1}$$

which implies

$$\rho = \frac{2\eta}{\xi^2+\eta^2}\,, \tag{A.2}$$

since $\rho = (x^2+y^2)^{1/2}$.

The scale factors $h_q = |\partial\boldsymbol{r}/\partial q|$ ($q = \eta,\, \xi,\, \phi$) involved in the expression of the gradient [44] are

$$h_\eta = \frac{2}{\xi^2+\eta^2}\,, \qquad h_\xi = \frac{2}{\xi^2+\eta^2}\,, \qquad h_\phi = \frac{2\eta}{\xi^2+\eta^2}\,, \tag{A.3}$$

such that the Jacobian of the transformation $(\xi,\eta,\phi) \mapsto (x,y,z)$ is

$$J = h_\eta h_\xi h_\phi = \frac{8\eta}{(\xi^2+\eta^2)^3}\,. \tag{A.4}$$

The basis unit vectors $\boldsymbol{e}_q = h_q^{-1}\,\partial\boldsymbol{r}/\partial q$ ($q = \eta, \xi, \phi$) are related to the Cartesian basis vector by the linear system

$$\boldsymbol{e}_\eta = \frac{\xi^2-\eta^2}{\xi^2+\eta^2}\cos\phi\,\boldsymbol{e}_x + \frac{\xi^2-\eta^2}{\xi^2+\eta^2}\sin\phi\,\boldsymbol{e}_y - \frac{2\eta\xi}{\xi^2+\eta^2}\,\boldsymbol{e}_z, \tag{A.5}$$

$$\boldsymbol{e}_\xi = -\frac{2\eta\xi}{\xi^2+\eta^2}\cos\phi\,\boldsymbol{e}_x - \frac{2\eta\xi}{\xi^2+\eta^2}\sin\phi\,\boldsymbol{e}_y + \frac{\eta^2-\xi^2}{\xi^2+\eta^2}\,\boldsymbol{e}_z, \tag{A.6}$$

$$\boldsymbol{e}_\phi = -\sin\phi\,\boldsymbol{e}_x + \cos\phi\,\boldsymbol{e}_y. \tag{A.7}$$

As the problem is axisymmetric, we also need the expressions of the Jacobian matrix of the transformation $(\rho,\phi,z) \mapsto (\eta,\xi,\phi)$ and the relationship linking the basis unit vectors. Since $\boldsymbol{e}_\rho = \cos\phi\,\boldsymbol{e}_x + \sin\phi\,\boldsymbol{e}_y$, one can see from eqs. (A.5) and (A.6) that

$$\boldsymbol{e}_\rho = \frac{\xi^2-\eta^2}{\xi^2+\eta^2}\,\boldsymbol{e}_\eta - \frac{2\eta\xi}{\xi^2+\eta^2}\,\boldsymbol{e}_\xi, \tag{A.8}$$

$$\boldsymbol{e}_z = -\frac{2\eta\xi}{\xi^2+\eta^2}\,\boldsymbol{e}_\eta + \frac{\eta^2-\xi^2}{\xi^2+\eta^2}\,\boldsymbol{e}_\xi. \tag{A.9}$$

Note that the derivative of the azimutal unit vector $\boldsymbol{e}_\phi$ with respect to ϕ can be immediately expressed as a function of the touching-sphere coordinates and unit vectors, since $\mathrm{d}\boldsymbol{e}_\phi/\mathrm{d}\phi = -\boldsymbol{e}_\rho$.

Finally, from the third equation of (A.1) and eq. (A.2), one gets the Jacobian matrix of the transformation $(\eta,\xi,\phi) \mapsto (\rho,\phi,z)$ and its inverse

$$\frac{\partial(\rho,z)}{\partial(\xi,\eta)} = \tfrac{2}{(\xi^2+\eta^2)^2}\begin{pmatrix} -2\eta\xi & \xi^2-\eta^2 \\ \eta^2-\xi^2 & -2\eta\xi \end{pmatrix}, \tag{A.10}$$

$$\frac{\partial(\xi,\eta)}{\partial(\rho,z)} = \tfrac{1}{2}\begin{pmatrix} -2\eta\xi & \eta^2-\xi^2 \\ \xi^2-\eta^2 & -2\eta\xi \end{pmatrix}. \tag{A.11}$$

Appendix A.2. Auxiliary translational flow and viscous drag

The Stokes streamfunction ψ for the translational motion of two unequal touching spheres along their centerline was derived by Cooley and O'Neil [33]. In terms of tangent-sphere coordinates its expression is given by

$$\hat{\psi} = \frac{\eta}{\xi^2+\eta^2}\,I(\xi,\eta), \tag{A.12}$$

with

$$I(\xi,\eta) = \int_0^\infty [(A+\xi C)\sinh s\xi + (B+\xi D)\cosh s\xi]\,\mathrm{J}_1(s\eta)\mathrm{d}s, \tag{A.13}$$

where A, B, C, D are functions of s and the geometry (*i.e.* of r only). We do not give the expressions of these constants since they are extremely cumbersome, but we give below the system to solve for them. Due to the choice we made for the non-dimensionalization, this system is different from the Cooley and O'Neil's one (eqs. (3.7)–(3.10) of ref. [33])[1]. Indeed, we chose the radius of the lower sphere (located in the $z < 0$ space) as the typical lengthscale so that the surface of the lower sphere is defined by $\xi = -1$ and the surface of the upper sphere by $\xi = \alpha = r^{-1}$. So A, B, C and D are solutions of the system

$$A\sinh s\alpha + B\cosh s\alpha + \alpha C\sinh\ s\alpha + \beta D\cosh s\alpha = -2\mathrm{e}^{-s\alpha}(\alpha + s^{-1}), \tag{A.14}$$

$$A\sinh s - B\cosh s - C\sinh s + D\cosh s = 2\mathrm{e}^{-s}(1 + s^{-1}), \tag{A.15}$$

$$A\cosh s\alpha + B\sinh s\alpha + C[s^{-1}\sinh s\alpha + \alpha\cosh s\alpha] + D[s^{-1}\cosh s\alpha + \alpha\sinh s\alpha] = 2\alpha\mathrm{e}^{-s\alpha}, \tag{A.16}$$

$$A\cosh s - B\sinh s - C[s^{-1}\sinh s + \cosh s] + D[s^{-1}\cosh s + \sinh s] = -2\mathrm{e}^{-s}. \tag{A.17}$$

The velocity components are obtained by applying the differential operator

$$\boldsymbol{D} = \frac{1}{r}\left[\frac{\partial}{\partial z}\,\boldsymbol{e}_\rho - \frac{\partial}{\partial \rho}\,\boldsymbol{e}_z\right], \tag{A.18}$$

to the streamfuction $\hat{\psi}$. The expression of $\boldsymbol{D}$ in terms of tangent-sphere coordinates can be derived using eqs. (A.8), (A.9) and (A.11), and one gets

$$\boldsymbol{D} = \frac{(\xi^2+\eta^2)^2}{4\eta}\left[\frac{\partial}{\partial \eta}\,\boldsymbol{e}_\xi - \frac{\partial}{\partial \xi}\,\boldsymbol{e}_\eta\right]. \tag{A.19}$$

Finally, velocity coordinates for the auxiliary flow $\hat{u} = \boldsymbol{D}\hat{\psi}$ are given by

$$\hat{u}_\xi = \frac{(\xi^2+\eta^2)^{1/2}}{4}\frac{\partial I(\xi,\eta)}{\partial \eta} + \frac{\xi^2 - 2\eta^2}{4\eta(\xi^2+\eta^2)^{1/2}}\,I(\xi,\eta), \tag{A.20}$$

$$\hat{u}_\eta = -\frac{(\xi^2+\eta^2)^{1/2}}{4}\frac{\partial I(\xi,\eta)}{\partial \xi} + \frac{3\xi\eta}{4\eta(\xi^2+\eta^2)^{1/2}}\,I(\xi,\eta). \tag{A.21}$$

The drag coefficient for each sphere is also given in eq. (4.3) of Cooley and O'Neil's original paper. After the summation of the two versions of eq. (4.3), the drag coefficient for the two spheres as a rigid body has the form

$$|\hat{\boldsymbol{f}}| = 2\pi\int_0^\infty sB\,\mathrm{d}s. \tag{A.22}$$

[1] Note that there is a typo in the sign of the fourth term on the right-hand side of eq. (3.8) in Cooley and O'Neil's original article.

Appendix A.3. Zeroth-order solution and advective term

The advective term can be easily derived since the only (azimutal) component of the viscous zeroth-order velocity is a function of ρ and z only. The Stokes solution $\boldsymbol{u}^{(0)} = u_\phi^{(0)}\,\boldsymbol{e}_\phi$ to the problem of two rotating touching spheres has been given by Takagi [34]. Considering the expression of the gradient in tangent-sphere coordinates[2] and knowing that $\mathrm{d}\boldsymbol{e}_\phi/\mathrm{d}\phi = -\boldsymbol{e}_\rho$, we can write

$$(\boldsymbol{u}^{(0)}\cdot\boldsymbol{\nabla})\,\boldsymbol{u}^{(0)} = \frac{{u_\phi^{(0)}}^2}{h_\phi}\left[\frac{\eta^2-\xi^2}{\xi^2+\eta^2}\,\boldsymbol{e}_\eta + \frac{2\eta\xi}{\xi^2+\eta^2}\,\boldsymbol{e}_\xi\right], \tag{A.23}$$

where

$$u_\phi^{(0)} = 2(\xi^2+\eta^2)\int_0^\infty\left[\frac{\sinh s(\xi+1)}{\sinh s(\alpha+1)}\mathrm{e}^{-s\alpha} + \frac{\sinh s(\alpha-\xi)}{\sinh s(\alpha+1)}\mathrm{e}^{-s}\right]s\mathrm{J}_1(s\eta)\mathrm{d}s. \tag{A.24}$$

Appendix A.4. Numerical integration

The numerical integration of expression (35) in the case of touching spheres is performed in the $(\xi,\,\eta)$ space using eqs. (A.4), (A.20), (A.21), (A.22) and (A.23). The space occupied by the fluid corresponds to the interval $[-1,\alpha]\times[0,+\infty]\times[0,2\pi]$. We discretized the range $[-1,\alpha]$ into 10^2 intervals. We also limited the interval of integration in the η-direction to the range $[10^{-5},10]$ (and divided it into 10^2 intervals as well) since i) the numerical integration could not be achieved for small values of η, ii) no difference was noticed in the result for upper boundaries greater than 10. The computation itself was done by means of the Legendre-Gauss Quadrature method [45].

Appendix B. Mathematics of separated spheres

Although the use of bispherical coordinates is more classical, we give in the following the same technical information as the one given for touching spheres for consistency.

Appendix B.1. Bispherical coordinates

The bispherical coordinate system (ξ,η,ϕ) is defined by the transformation

$$x = \frac{c\sin\eta\cos\phi}{\cosh\xi-\cos\eta}, \qquad y = \frac{c\sin\eta\sin\phi}{\cosh\xi-\cos\eta}, \qquad z = \frac{c\sinh\xi}{\cosh\xi-\cos\eta}, \tag{B.1}$$

[2] The general expression of the gradient operator in curvilinear coordinates is $\boldsymbol{\nabla} = \sum_q h_q^{-1}\,\partial_q\,\boldsymbol{e}_q$.

which implies

$$\rho = \frac{c \sin\eta \cos\phi}{\cosh\xi - \cos\eta}, \tag{B.2}$$

since $\rho = (x^2 + y^2)^{1/2}$. The prefactor c depends on the geometry. So, for radii ratio r and distance h, the dimensionless constant c is given by

$$c = \left[\frac{h^4 + (r^2-1)^2 - 2h^2(r^2+1)}{4h^2}\right]^{1/2}. \tag{B.3}$$

The surface of the upper (small) and lower (large) spheres are then given by $\xi = \alpha$ and $\xi = \beta$, with

$$\alpha = \sinh^{-1}\left(\frac{c}{r}\right) \qquad \text{and} \qquad \beta = -\sinh^{-1} c. \tag{B.4}$$

The scale factors $h_q = |\partial \boldsymbol{r}/\partial q|$ $(q = \eta, \xi, \phi)$ for the bispherical coordinate system are

$$h_\xi = \frac{c}{\cosh\xi - \cos\eta}, \qquad h_\eta = \frac{c}{\cosh\xi - \cos\eta},$$
$$h_\phi = \frac{c \sin\eta}{\cosh\xi - \cos\eta}, \tag{B.5}$$

such that the Jacobian of the transformation $(\xi, \eta, \phi) \mapsto (x, y, z)$ is

$$J = h_\eta h_\xi h_\phi = \frac{c^3 \sin\eta}{(\cosh\xi - \cos\eta)^3}. \tag{B.6}$$

Similar to the case of touching spheres, we need the expressions of the unit basis vectors for the cylindrical system and the Jacobian matrices of the transformation $(\eta, \xi, \phi) \mapsto (\rho, \phi, z)$ and its inverse. Knowing the expressions of the basis unit vectors for the bispherical coordinate system, one straightforwardly obtains the basis unit vector for the cylindrical coordinates system

$$\boldsymbol{e}_\rho = -\frac{\sinh\xi \sin\eta}{\cosh\xi - \cos\eta}\,\boldsymbol{e}_\xi + \frac{\cosh\xi\cos\eta - 1}{\cosh\xi - \cos\eta}\,\boldsymbol{e}_\eta, \tag{B.7}$$

$$\boldsymbol{e}_z = \frac{1 - \cosh\xi\cos\eta}{\cosh\xi - \cos\eta}\,\boldsymbol{e}_\xi - \frac{\sinh\xi\sin\eta}{\cosh\xi - \cos\eta}\,\boldsymbol{e}_\eta. \tag{B.8}$$

Finally, from the third term in eq. (B.1) and eq. (B.2), one gets the Jacobian matrix of the transformation $(\eta, \xi, \phi) \mapsto (\rho, \phi, z)$, which we can invert to obtain

$$\frac{\partial(\xi,\eta)}{\partial(\rho,z)} = \frac{1}{c}\begin{pmatrix} -\sinh\xi\sin\eta & \cosh\xi\cos\eta - 1 \\ 1 - \cosh\xi\cos\eta & -\sinh\xi\sin\eta \end{pmatrix}. \tag{B.9}$$

Appendix B.2. Auxiliary translational flow and viscous drag

The solution for separated spheres translating along their centerline was given by Stimson and Jeffrey [39] in the form of a discrete series

$$\hat{\psi} = (\cosh\xi - \cos\eta)\, S(\xi, \eta), \tag{B.10}$$

where

$$S(\xi,\eta) = \sum_{n=1}^{\infty} U_n(\xi) V_n(\eta), \tag{B.11}$$

with

$$U_n(\xi) = A_n \cosh(n - 1/2)\xi + B_n \sinh(n-1/2)\xi + C_n \cosh(n+3/2)\xi + D_n \sinh(n+3/2)\xi, \tag{B.12}$$

$$V_n(\eta) = P_{n-1}(\cos\eta) - P_{n+1}(\cos\eta). \tag{B.13}$$

In the expression of U_n, the constants A_n, B_n, C_n and D_n depend on the geometry of the system *i.e.* α and β as defined by (B.4). Their expression are given in Stimson and Jeffery's original article and are not reproduced here[3].

The expression of $\boldsymbol{D}$ (cf. sect. A.2) in terms of bispherical coordinates can be derived using (B.7), (B.8) and (B.9), and one gets

$$\boldsymbol{D} = \frac{(\cosh\xi - \cos\eta)^2}{c^2 \sin\eta}\left[\frac{\partial}{\partial\eta}\,\boldsymbol{e}_\xi - \frac{\partial}{\partial\xi}\,\boldsymbol{e}_\eta\right]. \tag{B.14}$$

Finally, velocity components for the auxiliary flow are given by

$$\hat{u}_\xi = \frac{(\cosh\xi - \cos\eta)^2}{c^2\sin\eta}\frac{\partial\hat{\psi}}{\partial\eta}, \tag{B.15}$$

$$\hat{u}_\eta = -\frac{(\cosh\xi - \cos\eta)^2}{c^2\sin\eta}\frac{\partial\hat{\psi}}{\partial\xi}, \tag{B.16}$$

where

$$\frac{\partial\hat{\psi}}{\partial\eta} = -\frac{3}{2}\frac{\sin\eta}{(\cosh\xi - \cos\eta)^{5/2}}\sum_{n=1}^{\infty} U_n V_n + (\cosh\xi - \cos\eta)^{3/2}\sum_{n=1}^{\infty} U_n \frac{\mathrm{d}V_n}{\mathrm{d}\eta}, \tag{B.17}$$

$$\frac{\partial\hat{\psi}}{\partial\xi} = -\frac{3}{2}\frac{\sinh\xi}{(\cosh\xi - \cos\eta)^{5/2}}\sum_{n=1}^{\infty} U_n V_n + (\cosh\xi - \cos\eta)^{3/2}\sum_{n=1}^{\infty} V_n \frac{\mathrm{d}U_n}{\mathrm{d}\eta}, \tag{B.18}$$

with

$$\frac{\mathrm{d}U_n}{\mathrm{d}\xi} = A_n(n-1/2)\sinh(n-1/2)\xi + B_n(n-1/2)\sinh(n-1/2)\xi + C_n(n+3/2)\sinh(n+3/2)\xi + D_n(n+3/2)\cosh(n+3/2)\xi, \tag{B.19}$$

$$\frac{\mathrm{d}V_n}{\mathrm{d}\eta} = (2n+1)\sin\eta P_n(\cos\eta). \tag{B.20}$$

[3] Note that the constant c is referred to as a in Stimson's original article [39].

The drag coefficient for each sphere is also given in Stimson and Jeffrey's paper (eqs. (34) and (35)). After the summation of these two equations, the drag coefficient for the two spheres as a rigid body has the form

$$|\hat{\boldsymbol{f}}| = -\frac{2^{5/2}}{c}\sum_{n=1}^{\infty}(2n+1)(A_n + C_n). \tag{B.21}$$

Appendix B.3. Zeroth-order solution and advective term

As in the case of the touching spheres, the advective term in the integrand of eq. (35) has to be expressed in terms of bispherical coordinates. The Stokes solution $\boldsymbol{u}^{(0)} = u_\phi^{(0)}\,\boldsymbol{e}_\phi$ to the problem of two rotating separated spheres was calculated by Jeffery [40]. Considering the expression of the gradient in tangent-sphere coordinates and knowing that (as in the previous case) $\mathrm{d}\boldsymbol{e}_\phi/\mathrm{d}\phi = -\boldsymbol{e}_\rho$, we have

$$(\boldsymbol{u}^{(0)}\cdot\boldsymbol{\nabla})\,\boldsymbol{u}^{(0)} = \frac{{u_\phi^{(0)}}^2}{h_\phi}\left[\frac{\sinh\xi\sin\eta}{\cosh\xi-\cos\eta}\,\boldsymbol{e}_\xi + \frac{1-\cosh\xi\cos\eta}{\cosh\xi-\cos\eta}\,\boldsymbol{e}_\eta\right], \tag{B.22}$$

where

$$u_\phi^{(0)} = (\cosh\xi-\cos\eta)^{1/2}\sum_{n=1}^{\infty}[H_n\cosh(n+1/2)\xi + G_n\sinh(n+1/2)\xi]\,P_n^1(\cos\eta), \tag{B.23}$$

with

$$H_n = \frac{2^{3/2}c}{\sinh(n+1/2)(\alpha+\beta)}\left[\mathrm{e}^{-(n+1/2)\alpha}\sinh(n+1/2)\beta + \mathrm{e}^{-(n+1/2)\beta}\sinh(n+1/2)\alpha\right], \tag{B.24}$$

$$G_n = -\frac{2^{3/2}c}{\sinh(n+1/2)(\alpha+\beta)}\left[\mathrm{e}^{-(n+1/2)\alpha}\cosh(n+1/2)\beta + \mathrm{e}^{-(n+1/2)\alpha}\cosh(n+1/2)\beta\right], \tag{B.25}$$

and where P_n^1 is the associated Legendre polynomial of order 1 and degree n.

Appendix B.4. Numerical integration

The numerical integration of eq. (35) in the case of separated spheres is performed in the (ξ,η,ϕ) space using eqs. (B.6), (B.15), (B.16), (B.21) and (B.22). The space occupied by the fluid corrsponds to the interval $[\beta,\alpha]\times[0,\pi]\times[0,2\pi]$. We discretized the range $[\beta,\alpha]$ into 10^2 intervals. We also limited the interval of integration in the η-direction to the range $[10^{-5},\pi]$ since the numerical integration could not be achieved for a lower boundary strictly equal to zero. The computation itself was done by mean of the Legendre-Gauss Quadrature method [45].

References

1. T.M. Squires, S.R. Quake, Rev. Mod. Phys. **77**, 977 (2005).
2. H.A. Stone, A.D. Stroock, A. Ajdari, Annu. Rev. Fluid Mech. **36**, 381 (2004).
3. A.D. Stroock, S.K.W. Dertinger, A. Ajdari, H.A. Stone, Science **25**, 647 (2002).
4. E.M. Purcell, Am. J. Phys. **45**, 3 (1977).
5. E. Lauga, T.R. Powers, Rep. Prog. Phys. **72**, 096601 (2009).
6. S.J. Ebbens, J.R. Howse, Soft Matter **6**, 726 (2010).
7. B.J. Nelson, I.K. Kaliakatsos, J.J. Abbott, Annu. Rev. Biomed. Eng. **12**, 55 (2010).
8. J. Wang, W. Gao, ACS-NANO **6**, 5745 (2012).
9. E. Lauga, Soft Matter **7**, 3060 (2009).
10. S. Childress, R. Dudley, J. Fluid Mech. **498**, 257 (2004).
11. N. Vandenberghe, J. Zhang, S. Childress, J. Fluid Mech. **506**, 147 (2004).
12. S. Alben, M. Shelley, Proc. Natl. Acad. Sci. U.S.A. **102**, 11163 (2005).
13. N. Vandenberghe, S. Childress, J. Zhang, Phys. Fluids **18**, 014102 (2006).
14. X.Y. Lu, Q. Liao, Phys. Fluids **18**, 098104 (2006).
15. E. Lauga, Phys. Fluids **19**, 061703 (2007).
16. D. Gonzalez-Rodriguez, E. Lauga, J. Phys.: Condens. Matter **21**, 204103 (2009).
17. S.E. Spagnolie, L. Moret, M.J. Shelley, J. Zhang, Phys. Fluids **22**, 041903 (2010).
18. G.I. Taylor, Proc. R. Soc. London, Ser. A **209**, 447 (1951).
19. E.O. Tuck, J. Fluid Mech. **31**, 301 (1968).
20. C. Brennen, J. Fluid Mech. **65**, 799 (1974).
21. A.S. Khair, N.G. Chisholm, Phys. Fluids **26**, 011902 (2014).
22. R.G. Cox, J. Fluid Mech. **23**, 625 (1965).
23. O.S. Pak, L. Zhu, L. Brandt, E. Lauga, Phys. Fluids **24**, 103102 (2012).
24. P. Tierno, R. Golestanian, I. Pagonabarraga, F. Sagués, Phys. Rev. Lett. **101**, 218304 (2008).
25. P. Tierno, R. Golestanian, I. Pagonabarraga, F. Sagués, J. Phys. Chem. B **112**, 16525 (2008).
26. P. Tierno, O. Guell, F. Sagués, R. Golestanian, I. Pagonabarraga, Phys. Rev. E **81**, 011402 (2010).
27. L. Zhu, E. Lauga, L. Brandt, Phys. Fluids **24**, 051902 (2012).
28. A.N. Whitehead, Q. J. Math. **23**, 143 (1889).
29. C.W. Oseen, Arkiv Mat., Astron. och Fysik **6**, 29 (1910).
30. H. Brenner, *Hydrodynamic Resistance of Particles at Small Reynolds Numbers*, Vol. **6** of *Adv. Chem. Eng.* (Academic Press, 1966) pp. 287–438.
31. W.G. Bickley, Philos. Mag. **25**, 746 (1938).
32. W.D. Collins, Mathematika **2**, 42 (1955).
33. M.D.A. Cooley, M.E. O'Neill, Proc. Camb. Philos. Soc. **66**, 407 (1969).
34. H. Takagi, J. Phys. Soc. Jpn. **36**, 875 (1974).
35. S. Kim, S.J. Karrila, *Microhydrodynamics* (Dover publication, Inc., 2005).
36. H. Brenner, R.G. Cox, J. Fluid Mech. **17**, 561 (1963).
37. R.G. Cox, H. Brenner, Chem. Eng. Sci. **23**, 147 (1968).
38. B.P. Ho, L.G. Leal, J. Fluid Mech. **65**, 365 (1974).
39. M. Stimson, G.B. Jeffery, Proc. R. Soc. London, Ser. A **111**, 110 (1926).

40. G.B. Jeffery, Proc. London Math. Soc. **14**, 327 (1915).
41. R.B. Bird, C.F. Curtiss, R.C. Armstrong, O. Hassager, *Dynamics of Polymeric Liquids*, Vol. **1** (Wiley-Interscience, New York, 1987).
42. F.A. Morrison, *Understanding Rheology* (Oxford University Press, New York, 2001).
43. S.E. Spagnolie, E. Lauga, Phys. Rev. Lett. **106**, 58103 (2011).
44. J. Happel, H. Brenner, *Low Reynolds number hydrodynamics* (Martinus Nijhoff Publishers, The Hague, 1983).
45. G. von Winckle, Legendre-Gauss Quadrature Weights and Nodes, `www.mathwork.com`.